Numerical method

$m\dot{\vec{v}} = v \times \vec{B} \longrightarrow \vec{u}' = \vec{u} \times \vec{B}$

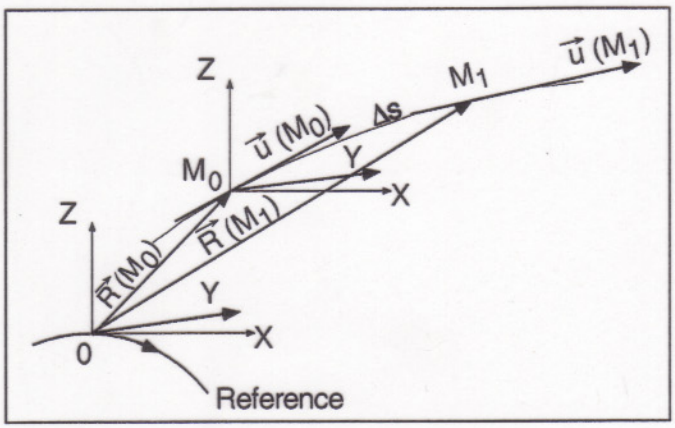

Fig. 1. Particle motion in the Zgoubi frame, and parameters used in the text.

Taylor.

$$\begin{aligned} \boldsymbol{R}(M_1) &= \boldsymbol{R}(M_0) + \boldsymbol{u}(M_0)\Delta s + \boldsymbol{u}'(M_0)\ \Delta s^2/2! + \ldots \\ \boldsymbol{u}(M_1) &= \boldsymbol{u}(M_0) + \boldsymbol{u}'(M_0)\Delta s + \boldsymbol{u}''(M_0)\ \Delta s^2/2! + \ldots \end{aligned}$$

wherein $\boldsymbol{u} = \boldsymbol{v}/v$ with $v = |\boldsymbol{v}|$, $ds = v\ dt$, $\boldsymbol{u}' = d\boldsymbol{u}/ds$, and with $m\boldsymbol{v} = mv\boldsymbol{u} = q\ B\rho\ \boldsymbol{u}$, $B\rho$ = rigidity of the particle with mass m and charge q. The derivatives $\boldsymbol{u}^{(n)} = d^n\boldsymbol{u}/ds^n$ are obtained as functions of the field derivatives $d^n\boldsymbol{B}/ds^n$, $d^n\boldsymbol{E}/ds^n$ by recursive differentiation of the equation of motion, in the following way.

Magnetic fields : In purely magnetic optical elements the particle rigidity is constant and the recursive differentiation simply writes $B\rho\ \boldsymbol{u}' = \boldsymbol{u} \times \boldsymbol{B}$, $B\rho\ \boldsymbol{u}'' = \boldsymbol{u}' \times \boldsymbol{B} + \boldsymbol{u} \times \boldsymbol{B}'$, and so forth.

Electrostatic fields : In purely electric fields the rigidity varies and the recursive differentiation takes the less simple form $(B\rho)'\boldsymbol{u} + B\rho\ \boldsymbol{u}' = \boldsymbol{E}/v$, $(B\rho)''\boldsymbol{u} + 2(B\rho)'\boldsymbol{u}' + B\rho\ \boldsymbol{u}'' = (1/v)'\boldsymbol{E} + \boldsymbol{E}'/v$, etc., whereas the rigidity itself is also obtained by Taylor expansion

$$(B\rho)(M_1) = (B\rho)(M_0) + (B\rho)'(M_0)\Delta s + (B\rho)''(M_0)\ \Delta s^2/2! + \ldots$$

The derivatives $(B\rho)^{(n)} = d^n(B\rho)/ds^n$ are in turn obtained by alternate recursive differentiation of, on the one hand $(B\rho)' = (\boldsymbol{e} \cdot \boldsymbol{u})/v$, and on the other hand $B\rho\ (1/v)' = (1/c^2)\ (\boldsymbol{e} \cdot \boldsymbol{u}) - (1/v)\ (B\rho)'$.

By principle these transformations are symplectic, in practice the Taylor series are truncated so that best precision is obtained when the higher order derivatives in the truncated series are zero (at least to machine accuracy) .

2.2 Field models

The major components in accelerators, at least relevant to DA studies, are multipoles or multipolar defects. Explicit analytical expressions of multipole fields and of their derivatives are drawn from the regular 3-D scalar potential (that

FIELD MAPS :

holds for both magnetic and (skew-) electric multipoles)

$$V_n(s,x,z) = (n!)^2\{\sum_{q=0}^{\infty}(-)^q\frac{\alpha_{n,0}^{(2q)}(s)}{4^q q!(n+q)!}(x^2+z^2)^q\}\{\sum_{m=0}^{n}\frac{\sin(m\frac{\pi}{2})x^{n-m}z^m}{m!(n-m)!}\} \quad (1)$$

$-\frac{\partial V_n}{\partial x} = -B_x$ —

where s, x, z coordinates are respectively curvilinear, transverse horizontal and vertical, $\alpha_{n,0}(s)$ $(n = 1,2,3,etc.)$ describe the longitudinal form of the field, including end fall-offs, and $\alpha_{n,0}^{(2q)} = d^{2q}\alpha_{n,0}/ds^{2q}$. Note that, within magnet body or as well when using hard edge field model, $d^{2q}\alpha_{n,0}/ds^{2q} \equiv 0$ $(\forall q \neq 0)$ hence the field and derivatives derive from the simplified potentials

$$V_1(x,z) = G_1 z\ , \qquad V_2(x,z) = G_2 xz\ , \qquad V_3(x,z) = G_3(x^2 - z^2/3)z, \quad \text{etc.} \quad (2)$$

where $G_n/B\rho$ is the strength.

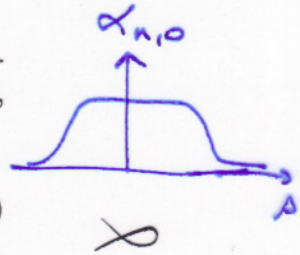

Field fall-off at magnet ends : As to the field fall-off on axis at magnet ends orthogonally to the effective field boundary (EFB), it is modeled by (after Ref. [10, page 240])

$$\alpha_{n,0}(d) = \frac{G_n}{1+\exp[P(d)]} \text{ with } P(d) = C_0 + C_1\frac{d}{\lambda_n} + C_2(\frac{d}{\lambda_n})^2 + \ldots + C_5(\frac{d}{\lambda_n})^5 \quad (3)$$

where d is the distance to the EFB and coefficients λ_n, $C_0 - C_5$ can be determined from prior matching with realistic numerical fringe field data.

More fields

Zgoubi is actually a genuine compendium of optical elements of all sorts, magnetic and/or electric, with fields derived from more or less sophisticated analytical models as above. This allows simulating with precision regular rings.

FIELD MAPS :

3D TOSCA

outputs

POISSON

≃ 1972

SPES 2 spectrometer

SATURNE 3GeV, p

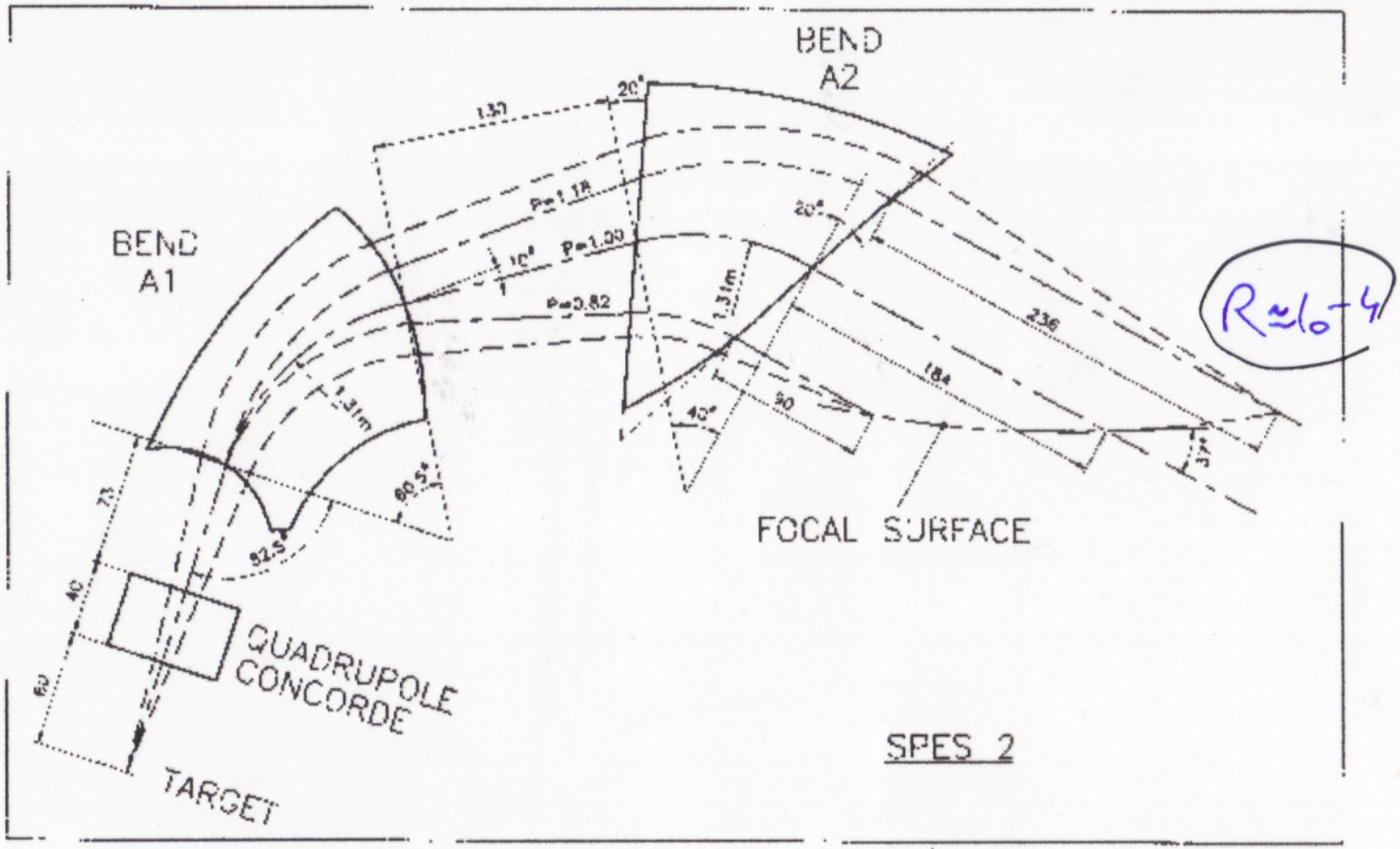

R≃10-4

≈ 1990

KAON BEAM, 800 MeV/c, BNL

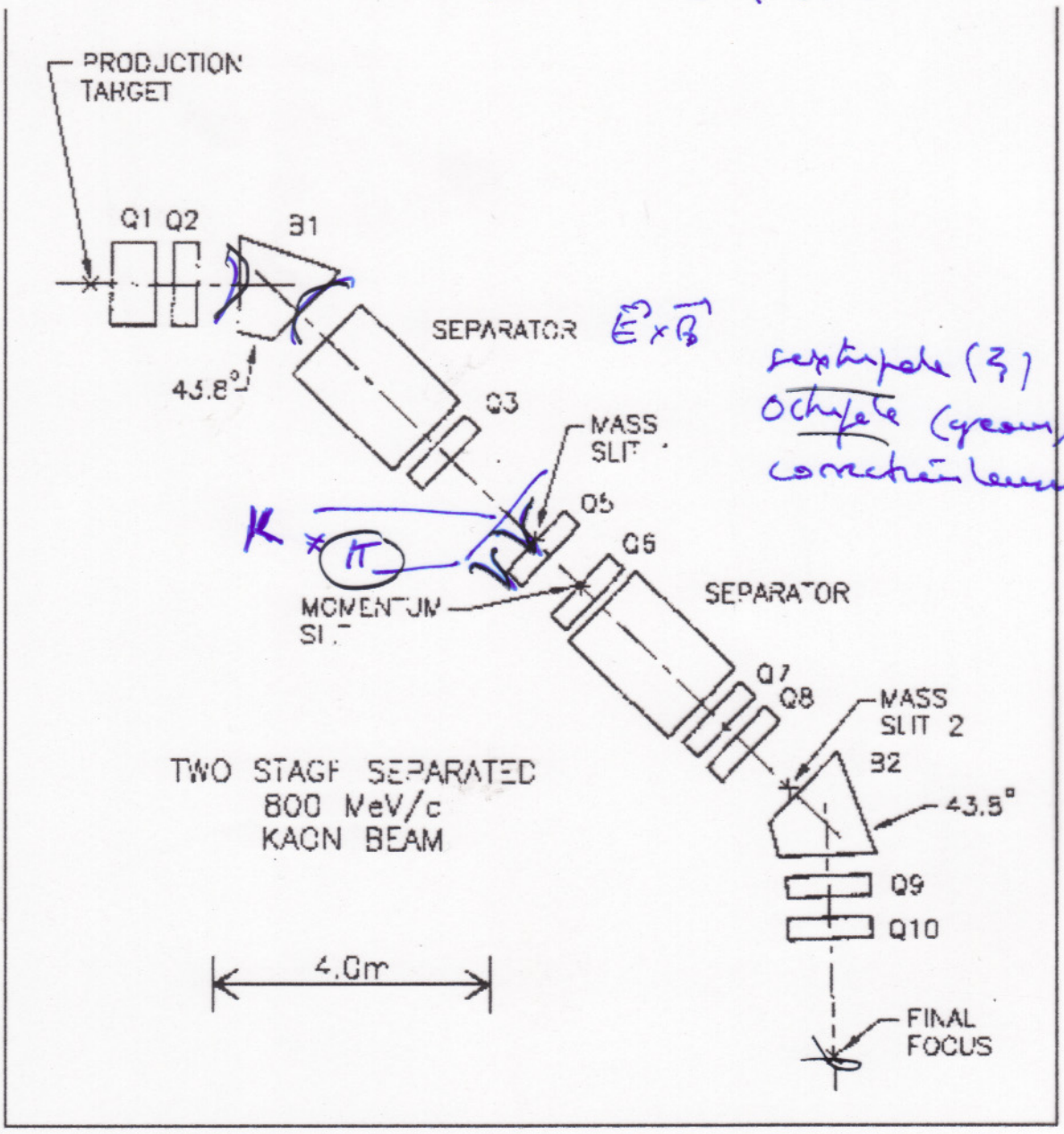

≃ 1992

SATURNE, PARTIAL SNAKE, IP, 4GeV → 3GeV

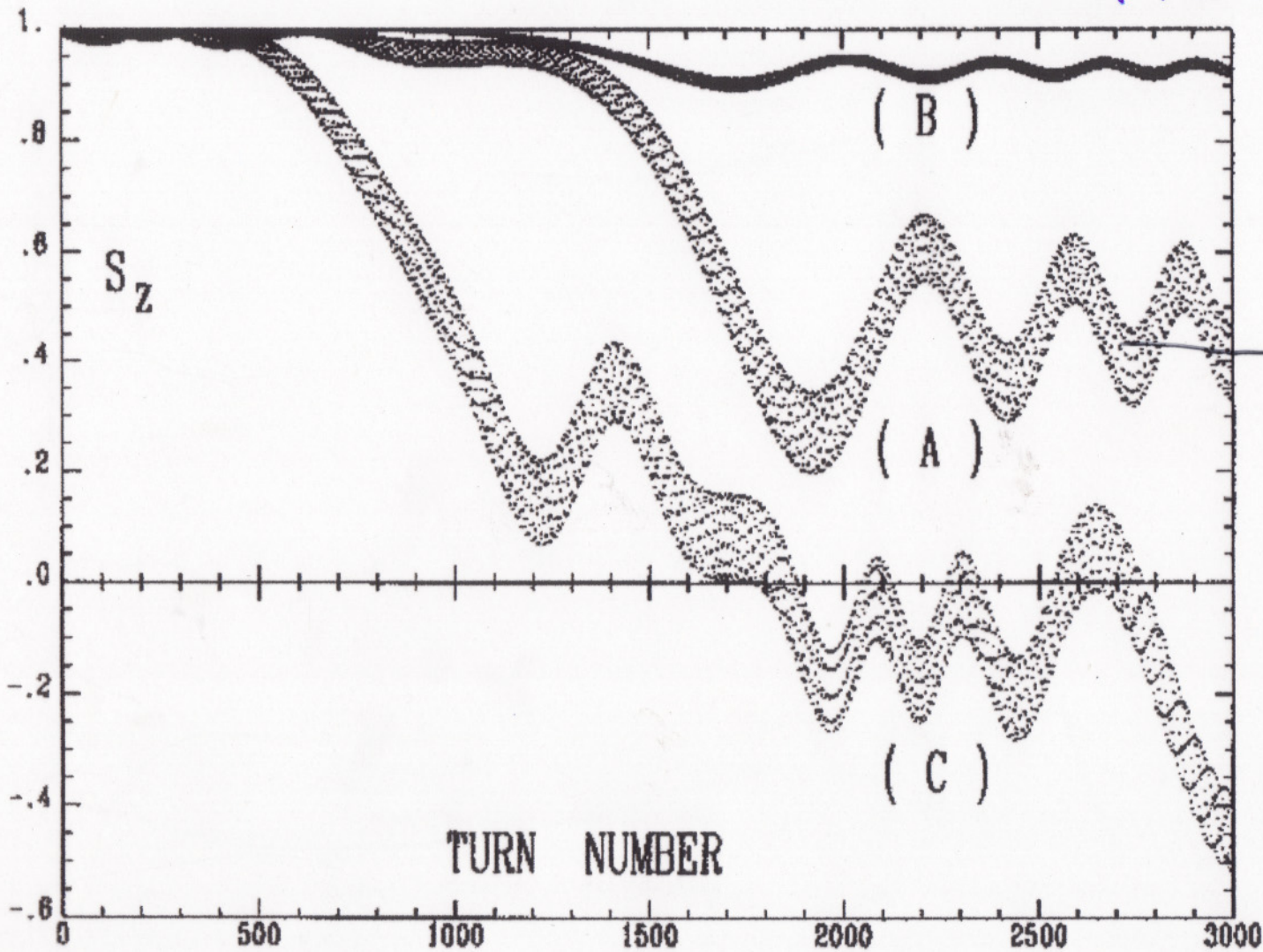

$\vec{\omega}' = \vec{\omega} \times \vec{B}$

$\vec{S}' = \vec{S} \times \vec{\omega}$

S_z ⌐ $\begin{vmatrix} S_x \\ S_y \\ S_z \end{vmatrix}$ ⇒ $|S| =$

good symplecticity, GJ

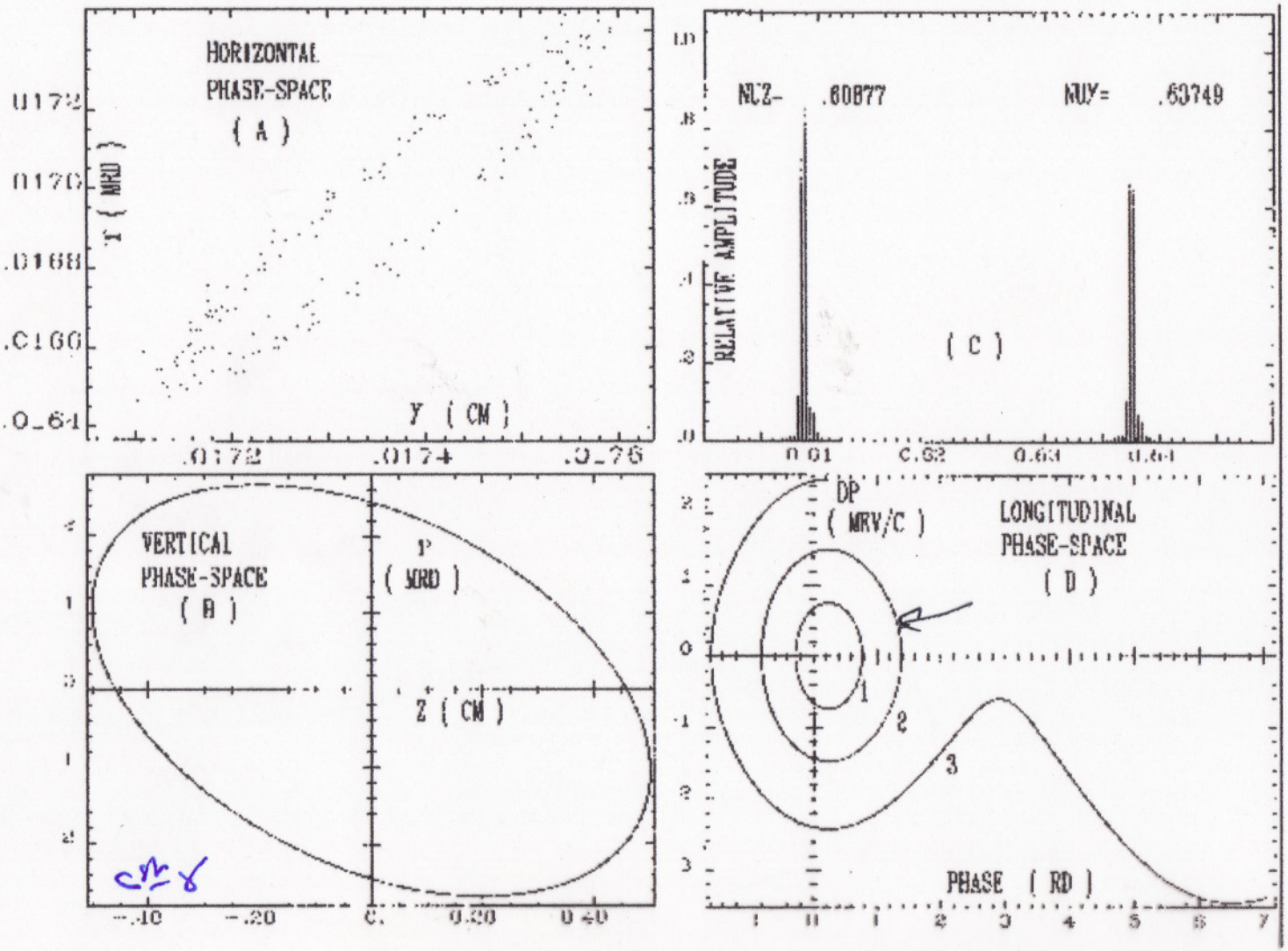

≈ 1996 3 DA tracking @ LHC, amongst other cases

In the following various results drawn from (unpublished) reports are presented, with the aim of showing the accuracy and effectiveness of the ray-tracing method.

3.1 Effect of b_{10} in low-β quadrupoles in LHC [5]

The multipole defect b_{10} in LHC low-β quadrupoles derives from (Eq. 1, Fig. 2)

b_{10} →

$$V_{10}(s,x,z) \approx \left(\alpha_{10,0} - \frac{\alpha''_{10,0}}{44}(x^2+z^2)\right)\left(10x^8 - 120x^6z^2 + 252x^4z^4 - 120x^2z^6 + 10z^8\right) \quad (4)$$

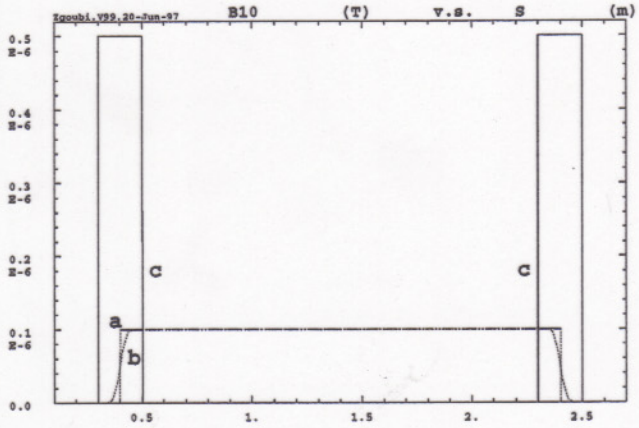

Fig. 2. Fringe field models used for assessing effect of b_{10} error on particle dynamics.

which b_{10} is zero in the body and the integral strength is shared between the two ends (c). In all three cases the overall field integral is the same.

Optical aberrations at IP5 : It can be seen from Fig. 3 that $b_{10} = -0.005\ 10^{-4}$ strongly distorts the aberration curves that would otherwise show a smooth, cubic shape. The aberration is of the form $x_{IP} \approx (\frac{x}{x'^3})x'^3_0 + (\frac{x}{x'^9})x'^9_0$ with x'_0 being the starting angle at point-to-point imaging location upstream of the interaction point (IP). The coefficient (x/x'^3) is mostly due to geometrical errors introduced

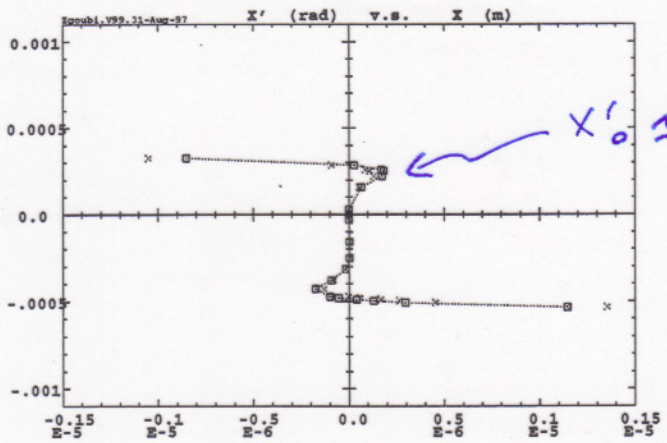

Fig. 3. Optical aberrations with inclined closed orbit at IP5 ($0.1\sqrt{2}$ mrad c.o. angle inclined 45°) ; fringe fields are set in separation dipoles D1/D2 and in the quadrupoles for the main component b_2. *Squares* : hard edge or fringe field model. *Crosses* : lump b_{10} model.

by the quadrupole and (x/x'^9) is due to b_{10} ; they have opposite signs and therefore act in opposite ways. The turn-round region between the two effects

gets closer to the x-axis the stronger b_{10}. In particular with the present value of b_{10} a ± 1 μm extent at the image is reached with starting angle within -10 to $15\,\sigma_{x'_0}$, about twice smaller than without b_{10}.

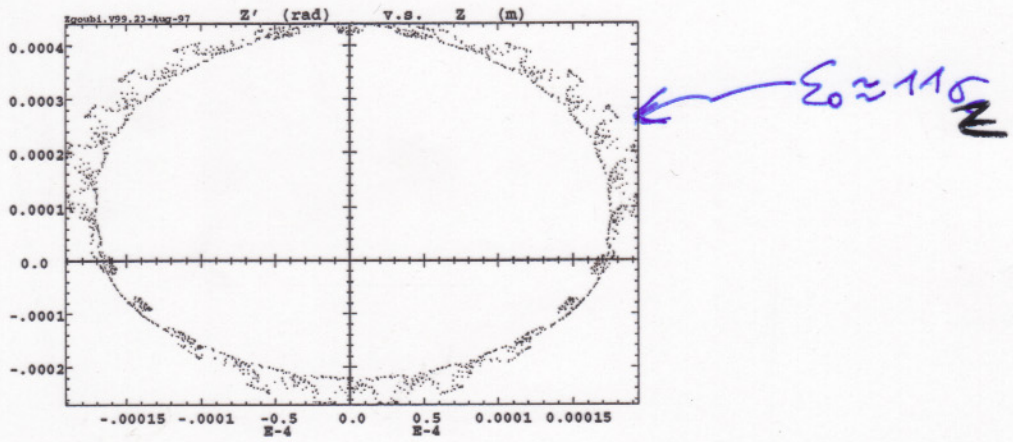

Fig. 4. Vertical phase space plot of a particle launched with x=x'=y=0 and $y' = 11.0\,\sigma$, in presence of inclined 0.28 mrad c.o. angles of identical signs at IP1 and IP5 simultaneously, with lumped b_{10} model (longitudinal distribution 'c' in Fig. 2).

DA tracking : Multiturn tracking of the dynamic aperture must stand the comparison. At first sight, considering the violent turn-round in the aberration curves (Fig. 3) and the fact that it occurs at $x'_0 \approx 9.5\,\sigma_{x'}$ whatever the longitudinal model for b_{10}, it can be expected that, on the one hand all three models provide similar DA, on the other hand the DA be about $9.5\,\sigma$ as well. This has been precisely confirmed by DA tracking, details can be found in Ref. [5]. As an illustration Fig. (4) provides a sample transverse phase space at 9.5σ DA.

illustration Fig. (4) provides a sample transverse phase space at exit [7].

3.2 Fringe field effects in the Fermilab 50 GeV muon storage ring [7]

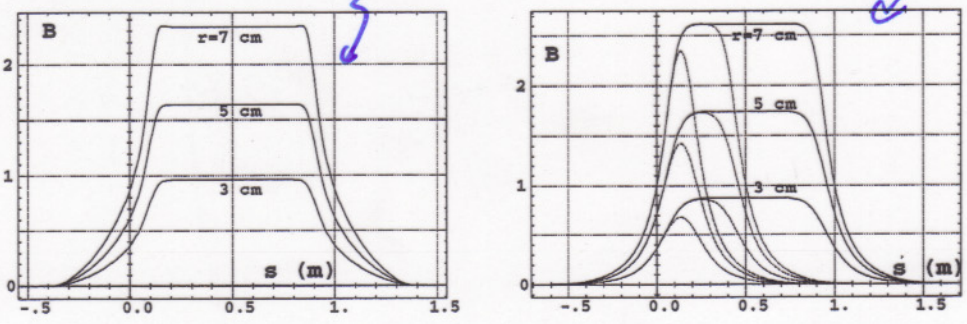

Fig. 5. Shape of the magnetic field $B(s)$ (arbitrary units) observed $3, 5$ or 7×10^{-2}m off-axis along the quadrupoles. Left : arc quadrupole (QF1, QD1 families) including sextupole component. Right : 1 m, 0.5 m or 0.27 m long matching quadrupoles.

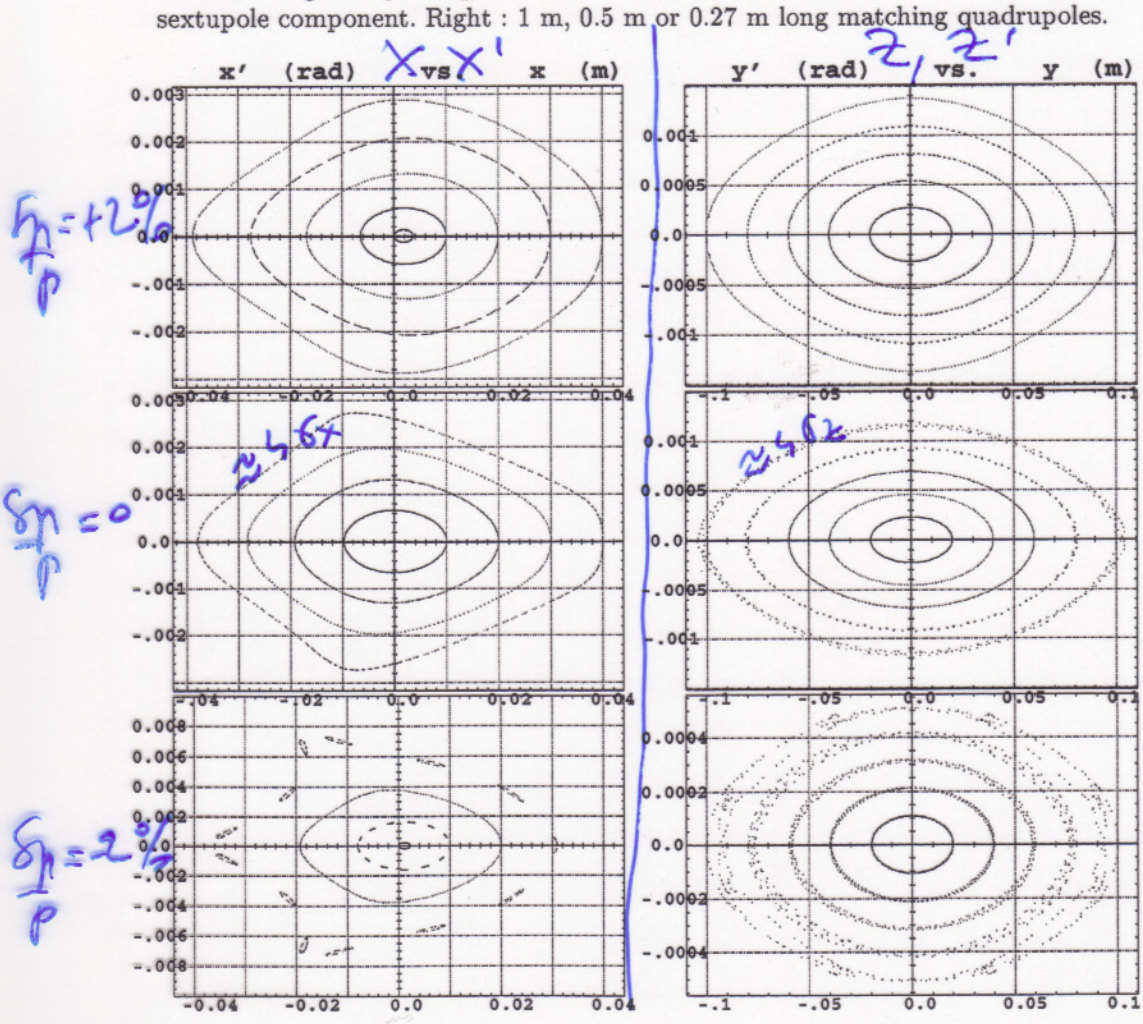

Fig. 6. Phase space plots up to DA region, no fringe fields, sextupoles are on. All particles survive except the largest amplitude one in the bottom left-hand plot (with initial conditions $x_0 = 0.04$ m $\approx 4\sigma_x$, $\delta p/p = -2\%$)

ntroduction

l tuning range (with phase trombone) in the Recycler ring [1] makes it worth disclosing all e sources of tune shifts and other alteration of machine parameters. In this respect, the study aims at describing effects of fringe fields present in the combined function dipoles. It rmed by means of the ray-tracing code Zgoubi which is based on stepwise solution of Lorentz n by a method of Taylor series. Aspects of the code relevant with this study are made clear more details can be found in Ref. [2]. A major feature of the method, of strong interest in n tracking as will be discussed later, is its ability to handle arbitrary magnetic fields with cally strong symplecticity. These issues have already been subject to meticulous investigations ious works, e.g. on the Saturne synchrotron [3] and on the LHC ring [4]. For instance the al tunes in the sharp edge field model are recovered at better than 10^{-4} in both cases, Saturne perimeter) : $\nu_x/\nu_y = 3.638574/3.620744$ from matrix transport, $\nu_x/\nu_y = 0.638564/0.620667$ y-tracing, and LHC (26700 m perimeter) : $\nu_x/\nu_y = 63.28000/63.31000$ from matrix transport, = 0.28006/63.31007 from ray-tracing. Such results give confidence in the ability of the ray- method to, on the one hand handle with precision such perturbations as end fields, on the and provide accurate computation of machine parameters.

Ray-tracing in the Recycler combined function dipoles

Multipole field

tangular combined function dipoles of the Recycler can be simulated with the built-in Mul- procedure of Zgoubi. The field and derivatives necessary for the Taylor-series based stepwise on of the Lorentz equation [2] are drawn from regular 3D scalar potential model [5] which in e of the dipole through sextupole components takes the respective forms

$$V_1(z,x,y) = \alpha_{1,0}(z)y - \frac{\alpha^{(2)}_{1,0}(z)}{8}(x^2+y^2)y + \frac{\alpha^{(4)}_{1,0}(z)}{192}(x^2+y^2)^2y - ... \quad (1)$$

$$V_2(z,x,y) = \alpha_{2,0}(z)xy - \frac{\alpha^{(2)}_{2,0}(z)}{12}(x^2+y^2)xy + \frac{\alpha^{(4)}_{2,0}(z)}{384}(x^2+y^2)^2xy - ... \quad (2)$$

$$V_3(z,x,y) = \frac{\alpha_{3,0}(z)}{3}(3x^2-y^2)y - \frac{\alpha^{(2)}_{3,0}(z)}{48}(3x^4+2x^2y^2-y^4)y + ... \quad (3)$$

he z, x, y coordinates are respectively longitudinal, transverse horizontal and vertical, $(n = 1, 2, 3)$ describes the longitudinal form $(x = y = 0)$(see Section 2.2) and $\alpha^{(2q)}_{n,0} = /dz^{2q}$. Note that, in the magnet body or as well when using a sharp edge field model, $/dz^{2q} \equiv 0$ (whatever $q \neq 0$) and hence the field and derivatives derive from the simplified als

$$V_1(x,y) = G_1 y,\ V_2(x,y) = G_2 xy,\ V_3(x,y) = G_3(3x^2-y^2)y/3 \quad (4)$$

he transverse gradients G_n are constant.

Fringe field model

d fall-off on axis at dipole ends orthogonally to the effective field boundary (*EFB*) is modeled . 240]

$$\alpha_{n,0}(d) = \frac{G_n}{1+exp[P(d)]},\ P(d) = C_0 + C_1\frac{d}{\lambda_n} + C_2(\frac{d}{\lambda_n})^2 + C_3(\frac{d}{\lambda_n})^3 \quad (5)$$

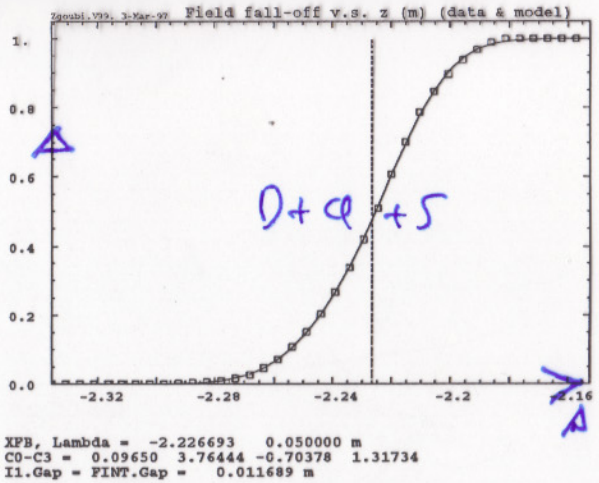

Figure 1: Field fall-off used for the simulation of the Recycler combined function dipole ends (the α_1, factor in Eq. (1)). The coefficients λ_1, $C_0 - C_3$ obtained by matching field data (squares) with the model (Eq. 5) are as displayed here and provide the solid line fall-off. The $\Pi \cdot gap$ value as used in simulations is also indicated. *XFB* is the position of the *EFB*, symbolized by the vertical dashed line

where d is the distance to the *EFB*, and the numerical coefficients λ_n, $C_0 - C_3$ are determined prior matching with numerical fringe field data. This is usually done in such a way that λ_1 *size* in which case one can take identical values $C_{0,1,2,3}$ for $n = 1-3$ while $\lambda_{2,3} \approx \lambda_1/2, \lambda_1/3$. T can be varied at will to possibly change or test the effect of the fall-off gradient, without affecti position of the *EFB* (i.e., without any effect on the magnetic length of the dipole). However we w $\lambda_1 = \lambda_2 = \lambda_3 =$ *gap size* for the combined function dipoles whose shape is closer to a regular geometry[1]. The fringe field used here is shown in Fig. 1 [8] which also displays the correspo matching Enge coefficients and the integral parameter $\Pi \cdot gap = \int \alpha_{n,0}(z)(1-\alpha_{n,0}(z))dz$ as u further MAD simulations [9, 10].

3 Sextupole free model

3.1 Magnet alignment ; orbit offset

Just like in the real world the magnets need be aligned in the Zgoubi data file. This is do specifying the position of the design orbit at magnet entrance and exit, which can be worked follows (see also [11]).

3.1.1 Sharp edge field model

Let (O,x,y,z) be the reference frame of the magnet (Fig. 2). Due to the transverse index $(\rho/B)(dB/dx)$ a particle traversing the rectangular combined function dipole experiences a constant bending, contrary to what would occur in a bent dipole with field index $(\rho/B)(dB$

[1] It has in fact been checked as to the quadrupole component [7] that the former rule $\lambda_2 \approx \lambda_1/2$ is the rig and it is believed that for the sextupole also, $\lambda_3 \approx \lambda_1/3$ is the right rule. Such differences in the gradients hav tested, they appear to have negligible effect.

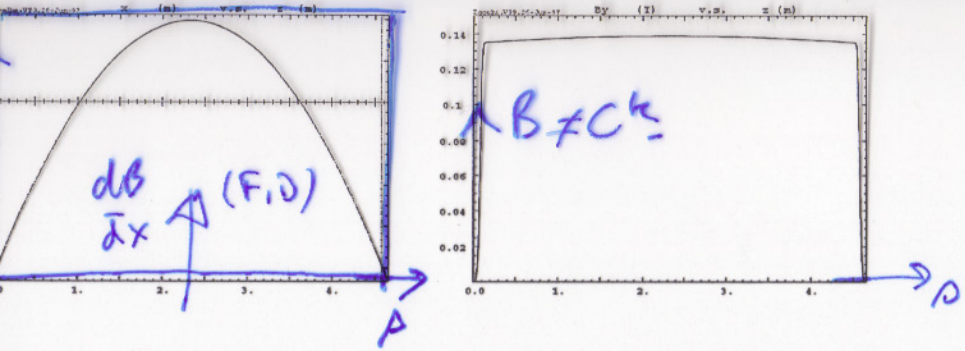

e 3: Left : horizontal trajectory of a particle entering ARCF at x_{off} under incidence $\theta/2$. Fringe do not make sensible difference. This path materializes the effective design orbit in the dipole. Right : tic field along the design orbit of an ARCF dipole including field fall-offs at both ends. The non nt field in the body is a combined effect of quadrupole index and bent trajectory. The vertical dashed epresent the EFB's.

513T T for $B\rho = 29.650\ Tm$). The difference between the circular path and the actual cosine-ajectory (Eq. 11) is discussed in App. B. The sagitta is obtained from (Eqs. 7, 8)

$$x(z) - x_{off} = \{(cos(z\sqrt{K}) - 1)\frac{1+C}{KS} + \frac{sin(z\sqrt{K})}{\sqrt{K}}\}\frac{\theta}{2} \quad (K \gtrless 0) \tag{12}$$

$= L_{mag}/2$ which leads to respectively 1.1775 10^{-2} m and 1.1664 10^{-2} m in ARCF and ARCD. comparison, the ray-tracing with sharp edge model provides identical values.

Horizontal motion with fringe fields

own in Ref. [6, pp. 243-244] the fringe field of a pure dipole does not induce any change izontal focusing, i.e., incoming parallel rays exit parallel ; this still holds in presence of the eld index in the Recycler dipole, as seen from the transfer matrices in Table 2 : the change izontal transfer coefficient from sharp edge to fringe field configuration is less than 5 10^{-4} ve). Another manifestation of fringe fields, of order zero, is to produce a displacement of the orbit inside the dipole with maximum amplitude [6, p. 244]

$$\Delta x \approx \Pi \cdot gap^2/\rho_{off} \tag{13}$$

stance in an ARCF (ARCD) dipole $\rho_{off} = B\rho/B_{off} \approx 219.8$ m (211.6 m) (Eq. 10 and Table 1), 5 10^{-2} m and $\Pi \cdot gap \approx 1.17\ 10^{-2}$ m (Fig. 1) which leads to $\Delta x \approx 2\ 10^{-6}$ m (3 10^{-6} m). Even ned with the transverse index this results in very small distortion of the design orbit, as shown osection 3.1.2 ; as a comparison with what precedes, the sagitta are unchanged (respectively 5 10^{-2} m and 1.1664 10^{-2} m in ARCF and ARCD). Considering such weakness of fringe field to zero and first order, possible higher order effects on the geometry can be neglected.

Vertical motion with fringe fields

ertical first order term due to the wedge angle is $\tan(\theta/2 - \psi)/\rho_{off}$ where ψ is the correction to the wedge angle which accounts for the effect of the fringe field ($\psi = 0$ with sharp edge) given by [6, p. 247]

Table 2: First order transfer matrices in the ARCF dipole (this is a sample, results are similar other types of dipoles). Note that, in ray-tracing with sharp edge field model the wedge effect in the motion is simulated by a wedge kick applied independently to each particle at entrance and exit MAD simulations are given in App. C for comparison. The agreement between ray-tracing and the sharp edge model is excellent : differences in transfer coefficient values do not exceed 1-2 unit last digit ; such small differences lead to less than 3.2 10^{-4} difference in fractional tune values as s Section 3.3.2 (Table 3). This is no longer the case in presence of fringe fields. The absence of any the adjustment to x^*_{off} is seen by comparison of the last two matrices.

ARCF
Sharp Edge

0.885868	4.323187	0.000000	0.000000
-0.049787	0.885868	0.000000	0.000000
0.000000	0.000000	1.118420	4.672315
0.000000	0.000000	0.053692	1.118420

Fringe field and x_off = 7.8426319361E-01

0.885819	4.323285	0.000000	0.000000
-0.049806	0.885818	0.000000	0.000000
0.000000	0.000000	1.118475	4.672209
0.000000	0.000000	0.053719	1.118475

Fringe field and x_off* = 7.83711560E-01

0.885818	4.323285	0.000000	0.000000
-0.049806	0.885818	0.000000	0.000000
0.000000	0.000000	1.118475	4.672209
0.000000	0.000000	0.053719	1.118475

$$\psi = \frac{\Pi \cdot gap}{\rho_{off}}(1 + sin^2\theta/2) \approx \frac{\Pi \cdot gap}{\rho_{off}}$$

Given $\rho_{off} \approx 215$ m, $\Pi \cdot gap \approx 1.17\ 10^{-2}$ m (Fig. 1) and with $\theta/2 \approx 10^{-3}$ rad, it comes $\psi \approx 5\ 1$ in ARCF/D dipoles. In other words the vertical focusing is but weakly affected by the fring as confirmed by transfer matrix calculations (Table 2).

3.3 Machine parameters

3.3.1 Closed orbit

Figure 4 shows the very small horizontal closed orbit excursion ($\approx \pm 4\ \mu m$) provided by t tracing in the sharp edge field model with design field $B_0 = 0.137513T$ T and with offset val from the cosine-like trajectory model (col. 3 of Table 1 and Eq. (8)). The Figure also sh negligible effect of fringe fields, as expected from Section 3.1 : the so increased excursion d exceed $\pm 0.04\ 10^{-3}$ m ; as shown in col. 5 of Table 1 x_{off} would have to be adjusted by le 5.5 μm in order to cancel it. In both cases the closed orbit is calculated from a 100-turn particle position at HMON and VMON monitors located as in MAD files [10].

3.3.2 Tunes

The tune values are computed either from a calculation of the full turn first order transfer obtained by ray-tracing of a set of paraxial rays over one machine turn, or from multiturn ray- and Fourier analysis of a single paraxial particle (launched on the invariants $\epsilon_x/\pi \approx \epsilon_y/\pi \approx 1$ m·rad at the start of the structure). Both methods give results similar at better than 5 10^{-6} (a value) such as displayed in Table 3.

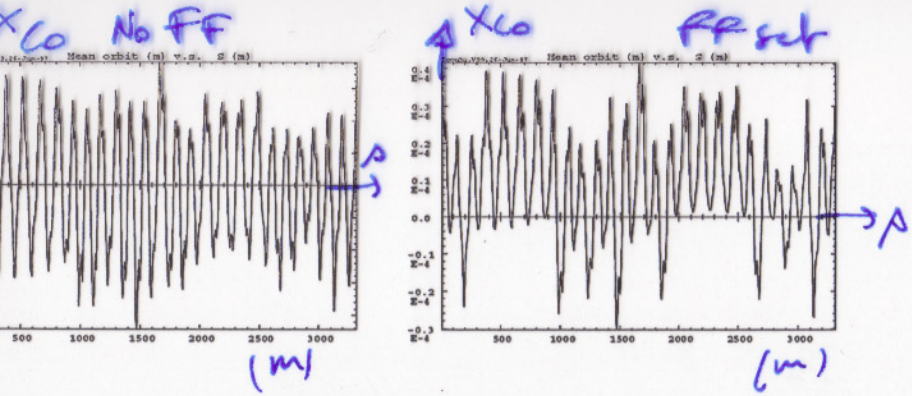

Left : closed orbit in the sharp model along the ring as recorded at HMON and VMON beam monitors. The horizontal axis displays monitor numbers. *Right* : closed orbit along the machine effect of fringe fields. Entrance offset is x_{off} in both cases (col. 3 of Table 1).

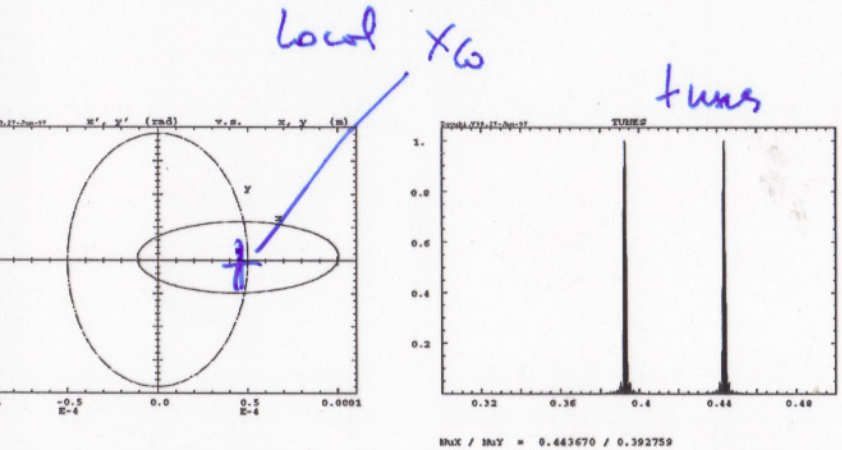

Left plot : 600 turns horizontal and vertical phase space ellipses at the beginning of the structure, tracing with fringe field model ; the particle is launched on the invariants $\epsilon_{x,y}/\pi \approx 10^{-10}$ m.rad. ntal closed orbit is a few tens of micrometers because the alignment value x_{off} is used (Eq. (7) and Table 1) ; using x^*_{off} instead (col. 5 of Table 1) would reduce it by about one order of magnitude. : Machine tunes in fringe field model, from Fourier analysis of the 600-turn tracking of the left limited sampling is cause of the non zero line width.

In the 1-turn matrix calculation, the symplecticity is checked through the horizontal and vert determinants. Namely, these differ from 1 by less than 10^{-8} in all tune calculations. In the 600-t tracking and Fourier analysis the symplecticity is checked through the smear of the invariant obtained by an ellipse matching of the phase space plots ; the smear is negligible, it does not exc $\sigma(\epsilon_{x,z}/\pi) \approx 5\ 10^{-3}$ m.rad (r.m.s.) in all tune calculations. Figure (5) shows an example of Fourier analysis data and post-processing in the fringe field model case.

MAD simulations are given for comparison (see also App. C). Note that, for the sake of c sistency these include some changes on MAD data namely, on the one hand RBEND with ler $L = \rho\theta$ instead of L_{mag}, on the other hand a corrected wedge angle so as to allow for the partic bend radius values at dipole ends - this is discussed in App. D.

Table 3 deserves some comments.

• The differences in tune from sharp edge to fringe field model observed with ray-tracing fit difference in the focusing terms in the transfer matrix (R_{21}, R_{43} coefficients, Table 2), as estim from $\Delta\nu = (1/4\pi)\int \beta\Delta K ds$ with $\beta \approx 50$ m and $\Delta(KL) \approx 2\ 10^{-5}$ in about 170 dipoles.

• As to the effect of fringe fields on the horizontal tune, they do not exist in matrix transp and they remain to be understood as to the ray-tracing method, most probably in terms of varyi values over the quadrupole fall-off, as occurs with pure quads in separate function focusing. Howe it can be checked that they are not due to the non-linearity introduced by the second order deriva $d^2\alpha_{1,0}/dz^2$ of the longitudinal form factor present in the dipole fringe field (Eq. 1), as follows : differentiation of Eq. (5) it comes $\Delta K \approx -x^2\ (d^2\alpha_{1,0}/dz^2)/(4B\rho) \approx 115\,Kx^2$, with $x \approx 8\ 10^-$ at magnet ends and hence, $\Delta\nu \approx \beta\Delta K\Delta s/4\pi \approx 7\ 10^{-6}$.

• As to the vertical tunes they also differ by $\approx 1.8\ 10^{-2}$ in fringe field model (in agreement v the $\approx 2.5\ 10^{-5}$ difference in the R_{43} transfer coefficient as mentioned above). In order to ob similar value with MAD, it appears that the effective parameter in this respect, $I1 \cdot gap$, would h to be changed by a non physical amount, therefore the reason for the difference is probably als the varying β values of the quadrupole fringe field.

Table 3: Machine tunes obtained by ray-tracing of paraxial rays. Tunes from MAD calculations are give rows 3,4, for comparison. The agreement in the sharp edge case is $\approx 3.3\ 10^{-4}$ (absolute) in both planes w "modified" (App. D) MAD simulation, which means that further comparisons are seated on a satisfac basis.

	Horizontal tune	Vertical tune
Ray-tracing		
Sharp edge	0.428015	*0.410913*[a]
Fringe field with x_{off}	0.443671	0.392760
Fringe field with x^*_{off}	0.443670	0.392762
MAD, modified[b]		
Sharp edge	25.428346	24.411267
Fringe field	25.428346	24.410859
MAD, original[c]		
Sharp edge	25.42700	24.409949
Fringe field	25.42700	24.408890

[a] Absence of fringe field is compensated by vertical wedge kick

[b] RBEND with $L = \rho\theta$ and modified wedge angles (Apps. C, D)

[c] See App. C [10]

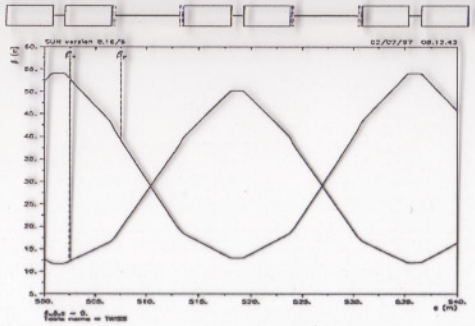

Figure 8: β functions in arc cell.

lots of analytical checks possible

E Appendix: Sextupole feed-down to quadrupole

imate the effect of sextupole feed-down on tunes in terms of $\Delta\nu = (1/4\pi)\int \beta \Delta K ds$. The
ns reach a maximum in any focusing type dipole (ARCF for horizontal motion and ARCD
l) and behave symmetrically in in a half-cell since there are 2 dipoles per half-cell (Fig. 8).
vs to write for both x and y motions

$$\beta(z) = cos^2(z\sqrt{(K)})\beta_{max} + sin^2(z\sqrt{(K)})/\beta_{max} \quad (K \gtrless 0) \tag{20}$$

focusing dipole. After some algebra, and neglecting the effect of defocusing type dipoles
the vertical plane and ARCD in the horizontal) one gets

$$\Delta\nu \approx \frac{N}{4\pi}\int \beta(z)\Delta K(z)dz = \frac{2NH}{4\pi}\frac{C}{K}(\beta_{max} - \frac{1}{K\beta_{max}})\{\frac{2}{3}(1+\frac{C}{2}) - \frac{S}{L}\} \tag{21}$$

$cos(L\sqrt{K})$, K = quadrupole strength, H = sextupole strength. Given N=108 dipoles,
we get $\Delta\nu_x/\Delta\nu_y \approx 2.3\ 10^{-3}/3.8\ 10^{-3}$/ which is close to the change observed ($2.15\ 10^{-3}/3.1\ 10^{-3}$)
ing the sextupole index (Tables 3, 5).

ences

ilab Recycler ring TDR, G. Jackson Ed., FERMILAB-TM-1981, July 1996.

léot and S. Valéro, Zgoubi users' guide, Note CEA/DSM/LNS/GECA/97-43 and
MILAB-TM-2010, CEA-Saclay and FNAL, 1997.

éot, A numerical method for the ray-tracing of polarized beams, Proc. EPAC Conf. 1992.

éot, On the effects of fringe fields in the LHC ring, Part. acc., 1996, Vol. 55, pp.[329-
83-92 ; F. Méot, A. París, On the effect of high-β region fringe fields and multipole errors
IC, FNAL, 1997, to be published.

eleux, Compléments sur la physique des accélérateurs, DEA de Physique et Technologie
Grands Instruments, rapport CEA/DSM/LNS/86-101, CEA, Saclay (1986).

Enge, Deflecting magnets, in *Focusing of charged particles*, volume 2, A. Septier ed.,
emic Press, New-York and London (1967).

[7] J.F. Ostiguy, personnal communication, BD/Phys., FNAL, 1997.

[8] Fringe field data provided by J.F. Ostiguy, BD/Phys., FNAL, 1997.

[9] H. Grote and F.C. Iselin, The MAD program V8.10, CERN/SL/90-13 (AP) (1993).

[10] MAd file rrv11d.lat, provided by J. Holt, BD/Phys., FNAL, 1997.

[11] N. Gelfand, Rectangular combined function magnets, Report MI-0200, FNAL, Jan. 1997.

[12] S. D. Holmes, Reference orbit trajectory in a combined function magnet, Report MI-0
FNAL, Dec. 1996.

CONCLUSION

FFAG OPTICS : SOUNDS

LIKE EXCITING ~~EXERCISE~~
STUDY